JOURNAL OF AIRCRAFT
Vol. 63, No. 5, September–October 2026

Synthesis of the Aerodynamic Model of a Flying Wing Aircraft

Salvatore Asaro* and Roelof Vos†
Delft University of Technology, 2629 HS Delft, The Netherlands

https://doi.org/10.2514/1.C038513

Flying-wing aircraft, such as the Flying V considered in this study, can substantially contribute to reducing the carbon footprint of the aviation sector. To enable adequate predictions regarding performance, stability, and control, a validated aerodynamic model of the Flying V is derived in this paper. The first part of the paper compares the aerodynamic coefficients determined with experiments and simulations conducted on a subscale version of the aircraft. The experiments are conducted in a wind tunnel and with flight tests, while the simulations are conducted using a vortex lattice method (VLM), a panel method, and a numerical method based on the Reynolds-averaged Navier–Stokes (RANS) equations. The comparison highlights the dependency of the aerodynamic coefficients on the angle of attack, which influences the flow acting on the aircraft. Based on the results of this comparison study, the full-scale aircraft aerodynamic model is derived by combining RANS and VLM simulations calibrated with experimental data. All aerodynamic coefficients are derived as a function of the angle of attack and at different Mach numbers and altitudes.

Downloaded by Technische Universiteit Delft on November 12, 2026 | http://arc.aiaa.org | DOI: 10.2514/1.C038513

Nomenclature

b	=	wingspan, m
C_D, C_L	=	drag and lift coefficients
CG	=	center of gravity, m
C_X, C_Y, C_Z	=	force coefficients along x, y, z
C_{X_α}	=	force coefficient along x due to α
$C_{X_{\delta_e}}$	=	force coefficient along x due to δ_e
C_{Y_β}	=	force coefficient along y due to β
C_{Y_r}	=	force coefficient along y due to r
$C_{Y_{\delta_a}}$	=	force coefficient along y due to δ_a
$C_{Y_{\delta_r}}$	=	force coefficient along y due to δ_r
C_{Z_α}	=	force coefficient along z due to α
C_{Z_q}	=	force coefficient along z due to $\hat{q}$
$C_{Z_{\delta_e}}$	=	force coefficient along z due to δ_e
C_{mx}, C_{my}, C_{mz}	=	moment coefficients around X, Y, Z
$C_{mx,p}$	=	rolling moment coefficient due to $\hat{p}$
$C_{mx,q}$	=	rolling moment coefficient due to $\hat{q}$
$C_{mx,r}$	=	rolling moment coefficient due to $\hat{r}$
$C_{mx,\beta}$	=	rolling moment coefficient due to β
C_{mx,δ_a}	=	rolling moment coefficient due to δ_a
C_{mx,δ_r}	=	rolling moment coefficient due to δ_r
$C_{my,\alpha}$	=	pitching moment coefficient due to α
C_{my,δ_e}	=	pitching moment coefficient due to δ_e
$C_{mz,\beta}$	=	yawing moment coefficient due to β
$C_{mz,p}$	=	yawing moment coefficient due to $\hat{p}$
$C_{mz,p}$	=	yawing moment coefficient due to $\hat{r}$
C_{mz,δ_a}	=	yawing moment coefficient due to δ_a
C_{mz,δ_r}	=	yawing moment coefficient due to δ_r
$\bar{c}$	=	mean aerodynamic chord, m
h	=	altitude, m
MLW	=	maximum landing weight, N
MTOW	=	maximum takeoff weight, N
M_x	=	rolling moment, N · m
M_y	=	pitching moment, N · m
M_z	=	yawing moment, N · m
M_∞	=	freestream Mach number
m	=	aircraft mass, kg
OEW	=	operating empty weight, N
p, q, r	=	angular velocity around x, y, z, rad/s
$\hat{p}$, $\hat{q}$, $\hat{r}$	=	dimensionless p, q, r
$Re_{\bar{c}}$	=	mean chord Reynolds number
S	=	wing reference area, m^2
U_∞	=	freestream velocity, m/s
X	=	force measured in the x direction, N
x	=	axis and coordinate along chord direction, m
Y	=	force measured in the y direction, N
y	=	axis and coordinate along span direction, m
y^+	=	dimensionless distance from the wall
Z	=	force measured in the z direction, N
z	=	axis and coordinate along vertical direction, m
α	=	angle of attack, deg
β	=	sideslip angle, deg
δ_a, δ_e, δ_r	=	aileron, elevator, and rudder deflection angles, deg
δ_f, δ_d	=	high-lift flap and droop nose deflection angles, deg
ρ_∞	=	freestream density, kg/m^3

Presented as Paper 2025-0852 at the AIAA SciTech 2025 Forum, Orlando, FL, January 6–10, 2025; received 11 April 2025; accepted for publication 8 December 2025; published online Open Access 13 February 2026. Copyright © 2025 by Salvatore Asaro and Roelof Vos. Published by the American Institute of Aeronautics and Astronautics, Inc., with permission. All requests for copying and permission to reprint should be submitted to CCC at www.copyright.com; employ the eISSN 1533-3868 to initiate your request. See also AIAA Rights and Permissions https://aiaa.org/publications/publish-with-aiaa/rights-and-permissions/.

*Postdoctoral Researcher, Faculty of Aerospace Engineering, Kluyverweg 1; s.asaro@tudelft.nl.

†Associate Professor, Faculty of Aerospace Engineering, Kluyverweg 1; r.vos@tudelft.nl. Associate Fellow AIAA (Corresponding Author).

I. Introduction

TUBE-AND-WING aircraft have been the standard configuration for commercial aviation. However, between 1990 and 2014, their fuel efficiency increased by approximately 10%, while the number of passengers and goods transported increased 2.5 times over the same period. By 2030, if the trend continues, the impact of aviation on greenhouse gas emissions will double [1]. To avoid this trend, the Advisory Council for Aeronautics Research in Europe (ACARE), with the Flightpath 2050 report, aims to reduce 75% CO_2 and 90% NO_x with respect to conventional aircraft from 2000 [2]. For these reasons, integrating new technologies into aircraft is being researched to reduce the weight and footprint of future aircraft [3]. A significant reduction in aircraft emissions could also be achieved by considering new aircraft types, such as Prandtl planes [4], blended wing bodies [5], or flying wings [6], which could increase the efficiency of the aviation sector by offering drag reduction compared to conventional aircraft. However, because of the lack of historical statistical data, the initial design phase of an aircraft usually relies on low-fidelity tools for quickly estimating the aerodynamic model. The accuracy of these tools can be hard to estimate, particularly for unconventional aircraft. Hence, higher-fidelity simulations and experiments are crucial for an adequate design, particularly to predict unanticipated nonlinearities. For example,



Fig. 1 Artist impression of the Flying V aircraft.

nonlinearities can occur in the forces and moments due to the angle of attack α and sideslip angle β, as well as a nonlinear change in control surface authority with α and β [7]. Additionally, new aircraft could rely on different control surfaces for flight control, such as drag rudders or spoilers [8], which induce separation on the wing. Hence, low-fidelity tools struggle to predict their impacts on forces and moments.

In this work, the Flying V™[‡] [9], a flying-wing aircraft, is considered. An artist's impression of the Flying V is depicted in Fig. 1. The Flying V aircraft geometry considered here, excluding engines, pylons, landing-gear fairings, and excrescences, at cruise conditions shows a maximum lift-to-drag ratio of 24.2 [10]. An independent study conducted on a comparable Flying V geometry has shown a maximum lift-to-drag ratio of 25.2 [11].

Several studies have numerically determined an aerodynamic model for such aircraft [12,13], employing low-fidelity tools such as vortex lattice methods and panel methods, which lack the ability to predict nonlinearities anticipated by wind tunnel experiments [14].

This work compares wind tunnel and flight test data with results from various numerical methods, such as the vortex lattice method (VLM), the panel method, and Reynolds-averaged Navier–Stokes (RANS) simulations. Both experimental and numerical methods are introduced in Sec. II. Based on the results of the comparison between the different methods conducted in Sec. III, the most suitable methods for estimating the aerodynamic model of the aircraft are identified. Finally, the aerodynamic model of the full-scale Flying V is synthesized by combining RANS simulations and VLM simulations calibrated with experimental results in Sec. IV.

II. Methodology

The aerodynamic characteristics of the Flying V are studied using several methods. Scaled versions of the aircraft are experimentally tested in the wind tunnel and through flight tests (Sec. II.A). Different-fidelity methods (Sec. II.B) are compared with experimental results in Sec. III.

A. Experimental Aerodynamic Analysis

Two different types of experiments are conducted. The models employed are depicted in Figs. 2a and 2b. The former shows the wind tunnel setup, and the latter shows the flight test article. These two scaled test articles share the same geometry and dimensions, but the wind tunnel model is half the size of the flight model. They each have a scaling factor of 4.6% with respect to the full-scale aircraft. More details on the geometry can be found in [14].

The two models also share the same control surfaces, depicted in Figs. 3a and 3b. The control surface on the winglet is employed as a rudder. The control surface on the wing is employed as an elevator and as an aileron (i.e., an elevon). In reality, the elevon consists of three individual control surfaces that can move as one or individually. For most of the study, the elevon is considered as one, but in Sec. III.D the effect of the three individual surfaces is analyzed.

[‡]Flying V is a trademark of Fortescue. The Flying V design is owned by Fortescue, with UK and NL patents pending.

1. Flight Tests

Flight tests are conducted with the test article in Fig. 2b. The model has a wingspan $b = 3$ m, a wing surface area $S = 1.87$ m^2, and a mean aerodynamic chord $\bar{c} = 0.81$ m. Further details on the model and the instrumentation implemented are presented in [15]. The forces and moments are calculated with respect to $x = -1.23$ m in the experiment; accordingly, the same reference point is used in Secs. III.A–III with the other numerical and experimental methods.

The subscale test article is 4.6% of the full-scale aircraft, which is considered in Sec. IV; however, the two subscale and full-scale geometries are not exactly the same. The flight tests are conducted at a freestream velocity U_∞ between 25 and 35 m/s, with the angle of attack, α, varying between 0 and 10 deg and the sideslip angle, β, in the range of ± 5 deg. As introduced before, the model is equipped with elevons (Fig. 3a) and rudders (Fig. 3b). To define the location of the surfaces, a right-handed reference frame is used, with the z-axis pointing downward and the x-axis pointing forward. The origin of this coordinate system is at the nose of the aircraft. The control surface deflections are indicated as δ_e for elevator, δ_a for aileron, and δ_r for rudder, and they are varied between $\delta_e = \delta_a = \pm 5$ deg and $\delta_r = \pm 10$ deg. The elevator deflection is defined to be positive when moving in the positive z-direction, i.e., trailing-edge down. Aileron deflection on the starboard side is defined to be positive when moving in the negative z-direction, i.e., trailing-edge up, and on the port side when moving in the positive z-direction, i.e., trailing-edge down. For the rudders, the deflection is positive when moving in the positive y-direction, i.e., trailing edge to the starboard side. When aileron input is provided to the elevons, the antisymmetric deflection angle on either side of the wing is the same. To properly operate the model during the flight tests, α, β, and the control surface angles are kept within ranges for which the forces and moments acting on the airplane are expected to change linearly.

The aircraft eigenmotions are excited with 3-2-1-1 maneuvers [16]. Each maneuver is initiated with a multistep input on the control surfaces, followed by a settling time in which the eigenmotion damps out. Each maneuver activates the elevator, the aileron, or the rudder. Further details on the tests conducted and the procedure to estimate the aerodynamic coefficients are presented in [15]. It should be noted that in the study considered, a $C_{my,\dot{\alpha}}$ term was not identified. Further tests are underway to verify this finding.

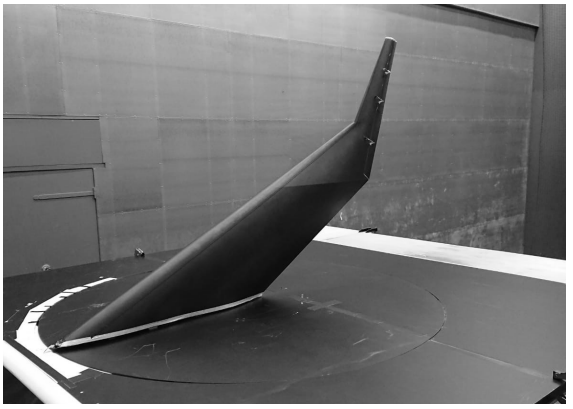
Table 1 summarizes the identified dependencies between force and moment coefficients, and angle of attack α, sideslip angle β, the control surface deflections (δ_e, δ_a, δ_r), and the dimensionless angular rates $\hat{p} = pb/(2U_\infty)$, $\hat{q} = q\bar{c}/(2U_\infty)$, and $\hat{r} = rb/(2U_\infty)$, where p, q, and r are the angular rates with respect to the x-, y-, and z-axis, respectively. A right-handed, body-fixed reference frame is used with the origin at the reference point (see Fig. 3a), the x-axis pointing forward, the y-axis in the direction of the starboard wing, and the z-axis pointing downward. The forces X, Y, and Z are measured in this body reference frame and align with the axes, x, y, and z, respectively. The moments M_x, M_y, and M_z are the rolling, pitching, and yawing moments, respectively, about the axes x, y, and z.

As mentioned earlier, the flight tests are conducted at relatively low α, β, δ_e, δ_a, and δ_r, for which forces and moments are expected to vary linearly. To study possible nonlinear effects, further tests are conducted in the wind tunnel (Sec. II.A.2), and the results from wind tunnel and flight tests are compared in Sec. III.A. However, the comparison features only the static aerodynamic coefficients because the impact of the angular rates on forces and moments cannot be determined through static wind tunnel measurements.

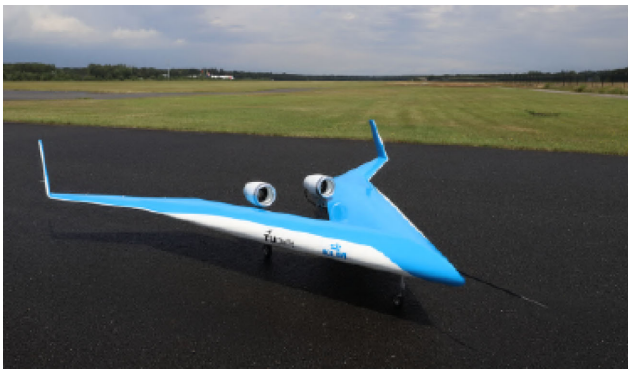
2. Wind Tunnel Tests

Wind tunnel experiments are conducted on the half model depicted in Fig. 2a. The $x - z$ plane is considered a symmetry plane; i.e., the wind tunnel model has a half-span and the same mean aerodynamic chord as the subscale flight model described in Sec. II.A.1. The tests are carried out at $U_\infty \simeq 25$ m/s and $M_\infty \simeq 0.07$, and the temperature is kept fixed with a heat management system, resulting in a Reynolds number with respect to the mean aerodynamic chord of $Re_{\bar{c}} = 1.3 \cdot 10^6$. Forces and moments

Downloaded by Technische Universiteit Delft on November 12, 2026 | http://arc.aiaa.org | DOI: 10.2514/1.C038513

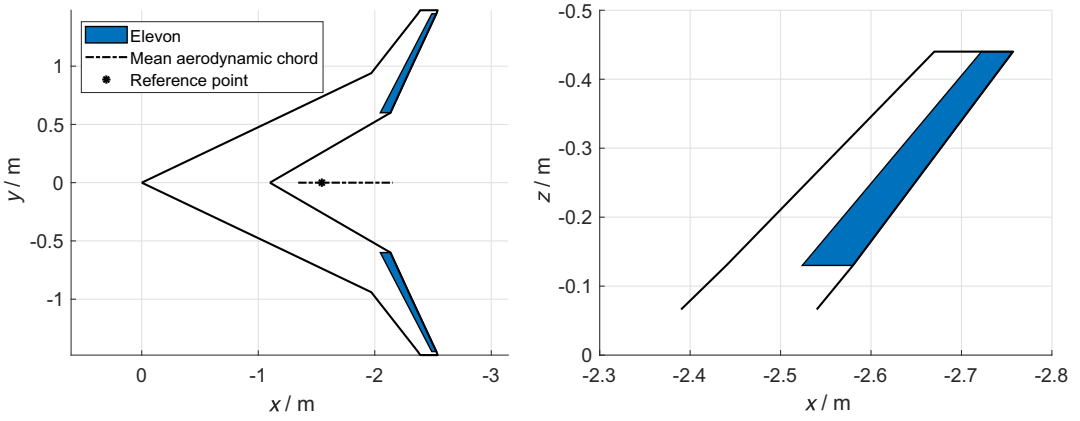


a) Wind tunnel model: $b/2 = 1.5$ m [14]



b) Flight test article: $b = 3.0$ m [15]

Fig. 2 Wind tunnel test article and flight test article of 4.6% scale.



a) Elevons on the subscale aircraft, top-view

b) Rudder on the winglet, side-view

Fig. 3 Control surfaces on subscale aircraft.

Table 1 Force and moment coefficient dependencies identified with flight tests

	α	β	$\hat{p}$	$\hat{q}$	$\hat{r}$	δ_e	δ_a	δ_r
C_X	x					x		
C_Y		x			x		x	x
C_Z	x			x		x		
C_{mx}		x	x		x		x	x
C_{my}	x			x		x		
C_{mz}		x	x		x		x	x

Note: All forces and moments are measured in the body reference frame.

acting on the half wing are measured with a six-component balance. The balance is mounted under a turning table that varies the angle of attack α. Furthermore, the wind tunnel test article has the same control surfaces as the subscale flight test article (Sec. II.A.1).

The wind tunnel tests allow measurement of the dependencies of force and moment from α, δ_e, δ_a, and δ_r, which can be tested over a wider range compared to the flight tests, allowing also the study of the change of the control surfaces' control authority with α.

B. Numerical Aerodynamic Analysis

The aerodynamic coefficient dependencies indicated in Table 1 are estimated with tools of varying fidelity presented herein. Numerical and experimental results are then compared in Sec. III to identify the tool or combination of tools that can be employed to derive the aerodynamic model of the full-scale aircraft (Sec. IV).

1. *Vortex Lattice Method*

The VLM is based on potential flow theory; i.e., the flow is incompressible and irrotational. The considered geometry, e.g., a wing, is discretized with panels. For each panel, a bound vortex is located at the 25% chord point, and a control point is located at the 75% chord point, where the flow tangency condition is imposed. The VLM does not include any viscous effects or wing thickness. Furthermore, it cannot predict transonic flow or crossflow, which can be significant for highly swept wings. The code employed in this study is Athena Vortex Lattice (AVL).

Table 2 summarizes the results of the mesh independence study conducted on three grids for C_X, C_Z, and C_{my}. In particular, the table shows the relative difference of C_X, C_Z, and C_{my} with respect to the

Table 2 VLM mesh independence study for subscale aircraft at $M_\infty = 0.07$ and various α

Mesh	α, deg	ΔC_X, %	ΔC_Z, %	ΔC_{my}, %
Coarse	0	8.2	0.22	−0.45
	10	−1.3	0.13	−0.54
	20	−1	0.0086	−0.63
Medium	0	4.1	0.1	−0.21
	10	−0.63	0.065	−0.25
	20	−0.51	0.029	−0.29
Fine	0	2.4	0.069	−0.14
	10	−0.37	0.04	−0.17
	20	−0.29	0.0007	−0.19

Δ is the difference with respect to the Richardson extrapolation value of C_X, C_Z, and C_{my}.

Downloaded by Technische Universiteit Delft on November 12, 2026 | http://arc.aiaa.org | DOI: 10.2514/1.C038513

extrapolated Richardson values, e.g., $\Delta C_X = C_X - C_{X,\text{Richardson}})/C_{X,\text{Richardson}}$. The number of elements of the coarse, medium, and fine grids is, respectively, 1350, 2700, and 5400, which, e.g., for the medium grid, corresponds to having 90 panels along the wingspan and 30 panels along the chord. For the three meshes, the panel distribution along the chord is finer in the leading- and trailing-edge areas. The mesh independence study is conducted at $\alpha = 0$, 10, and 20 deg, because this is the range of interest for the subscale aircraft, as will be discussed in Sec. III.C.

The results show that the difference decreases with an increasing number of elements, as expected. Higher differences are obtained for C_X at $\alpha = 0$ deg, where the values are close to zero. For the continuation of the study, the medium mesh is selected, for which the change in forces and moments as a function of angle of attack with respect to the Richardson extrapolated values is lower than 0.7%, excluding C_X at $\alpha = 0$ deg.

2. Panel Method

Similarly to the VLM, the panel method is based on potential flow, where the flow is supposed to be inviscid, incompressible, and irrotational. The considered geometry is discretized with panels, and in each panel is allocated a singularity, specifically surface vorticity. Differently from the VLM, the wing thickness is considered by independently discretizing the upper and lower surfaces, and the primary variables solved are the strengths of these vortex panels. The simulations are conducted with Flightstream, which, in addition to common panel methods, also includes compressibility models and coupled integral boundary-layer models that approximate the shedding of vorticity into a viscous wake system [17].

The total number of panels is selected after a grid independence study conducted on the subscale aircraft geometry, similarly to the study conducted with the VLM in Sec. II.B.1. Table 3 summarizes the results of the mesh independence study conducted on three grids for C_X, C_Z, and C_{my} and at three different angles of attack. The number of elements of the coarse, medium, and fine grids is, respectively, 8190, 16,380, and 32,760, which, e.g., for the medium grid, corresponds to having 180 panels along the wingspan and 91 panels along the chord. For the three meshes, the panel distribution along the chord is finer in the leading- and trailing-edge areas.

The results show that the difference decreases with an increasing number of elements, as expected. Higher differences are obtained for C_X at $\alpha = 0$ deg, where the values are close to zero. For the continuation of the study, the medium mesh is selected, for which the change in forces and moments as a function of angle of attack with respect to the Richardson extrapolated values is lower than 0.8%, excluding C_X at $\alpha = 0$ deg.

3. Reynolds-Averaged Navier–Stokes Equations

The RANS simulations are solved with Ansys Fluent, which solves the equations with a finite volume method. A density-based approach is used with an implicit formulation and the Monotonic Upstream-Centered Scheme for Conservation Laws (MUSCL) for spatial discretization. A least-squares cell-based method with a third-order MUSCL scheme minimizes numerical diffusion. The $k-\omega$ shear stress transport ($k-\omega$ SST) is employed as the turbulence model.

Table 3 Panel method mesh independence study for subscale aircraft at $M_\infty = 0.07$ and various α

Mesh	α, deg	ΔC_X, %	ΔC_Z, %	ΔC_{my}, %
Coarse	0	−2.6	−1.4	−0.52
	10	1.3	0.76	0.23
	20	1.2	0.69	−1.2
Medium	0	−1.4	−0.76	−0.32
	10	0.77	0.42	0.13
	20	0.72	0.45	−0.68
Fine	0	−0.95	−0.49	−0.16
	10	0.44	0.26	0.076
	20	0.38	0.21	−0.44

Δ is the difference with respect to the Richardson extrapolation value of C_X, C_Z, and C_{my}.

Table 4 Number of cells and y^+ used for the mesh independence study of the subscale and full-scale aircraft

Scale	Mesh	Airfoil	Span	y^+	Inner	Total cells $\times 10^6$
Subscale	Coarse	180	81	0.75	114	3.2
	Medium	224	100	0.6	143	6.4
	Fine	280	125	0.5	180	12.9
Full-scale	Coarse	178	144	0.5	127	6.1
	Medium	224	182	0.4	156	12.1
	Fine	280	229	0.3	200	24.1

The meshes for the 3D RANS simulations are created with ICEM-CFD. The grids employed in this study consist of quadratic elements, and the grid is selected after a mesh independence study. The characteristics of the tested grids are summarized in Table 4. Different grids are created for the subscale and full-scale aircraft tested in this work. However, a similar meshing strategy is followed for both cases.

For both aircraft, three different meshes, labeled coarse, medium, and fine, are considered, with a total number of cells that doubles for both the subscale and full-scale aircraft. Table 4 shows the number of elements on the airfoil, along the span, and in the region close to the aircraft, labeled inner. The inner region extends along z to a height of at most 40% of the local chord c, as depicted in Fig. 4. The first dimensionless element height y^+ is calculated for the subscale aircraft at $M_\infty = 0.07$ and at $M_\infty = 0.85$ for the full-scale aircraft. The height of the elements grows with an expansion ratio of 1.1 for both aircraft. The far field is modeled as a semisphere with the symmetry plane coinciding with the aircraft symmetry plane. The nose of the aircraft is located at the center of the symmetry plane, and the semisphere has a radius of approximately $120\bar{c}$. The number of elements and the y^+ values for the different grids are chosen expecting the formation of vortices, particularly at higher angles of attack.

Table 5 summarizes the mesh independence study for the subscale aircraft. The simulations are conducted at wind tunnel conditions, i.e., $M_\infty = 0.07$ and $Re_{\bar{c}} = 1.3 \cdot 10^6$, similarly to the studies conducted to choose the grid for the VLM and panel method in Secs. II.B.1 and II.B.2.

The three grids are tested at $\alpha = 0$, 10, and 20 deg, which is the range of interest for the subscale aircraft, as will be discussed in Sec. III.C; additionally, higher angles of attack than the cruise α are chosen to verify whether the results are mesh independent also when more complex flow develops on the wing.

Table 5 shows the relative difference of C_X, C_Z, and C_{my} with respect to the extrapolated Richardson values. The results show that the difference decreases with an increasing number of elements, as expected. Higher relative differences are noted for $\alpha = 0$ deg, where the values of the force and moment coefficients are close to zero. This relative difference is particularly high for C_{my}. For the continuation of the study, the medium mesh is used because of the relatively small difference with respect to the Richardson value, and, as will be shown in Sec. III.C, the simulation results closely match the experimental data.

Table 6 summarizes the mesh independence study for the full-scale aircraft. The simulations are conducted at two flight conditions, i.e., $M_\infty = 0.2$ and $M_\infty = 0.85$, which correspond to $Re_{\bar{c}} = 8.4 \cdot 10^7$ and $11.1 \cdot 10^7$, for altitudes of $h = 0$ m and $h = 11$ km, respectively. At subsonic conditions, the tested angles of attack are 0, 10, and 20 deg. At cruise conditions $\alpha = 0$, 5, and 10 deg. The angle-of-attack ranges for the subsonic and transonic conditions are chosen according to the range employed in Sec. IV.

A similar trend to that of the mesh independence study of the subscale aircraft can be noticed. However, larger differences between meshes can be observed at higher Mach numbers due to the presence of shock waves on the outer wing. The runtimes of the medium and fine meshes are, respectively, approximately 1.9 and

Downloaded by Technische Universiteit Delft on November 12, 2026 | http://arc.aiaa.org | DOI: 10.2514/1.C038513

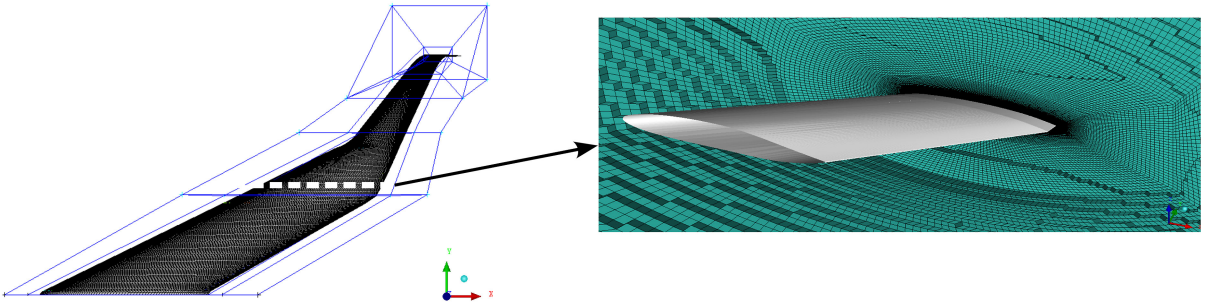


Fig. 4 Distribution of elements and inner block, and plane with mesh around the subscale aircraft for medium grid. Similar strategy employed for the full scale.

Table 5 RANS mesh independence study for subscale aircraft at $M_\infty = 0.07$ and various α

Mesh	α, deg	ΔC_X, %	ΔC_Z, %	ΔC_{my}, %
	0	1.6	6.8	17.9
Coarse	10	−6.5	−1.5	−2.6
	20	−3.4	2.1	4.2
	0	1.1	4.1	11.1
Medium	10	−4.8	−1.2	−1.7
	20	−2.2	1.3	2.8
	0	0.6	2.2	6.9
Fine	10	−3.5	−0.89	−1.2
	20	−1.4	0.8	1.8

Δ is the difference with respect to the Richardson extrapolation value of C_X, C_Z, and C_{my}.

Table 6 RANS mesh independence study for full-scale aircraft at $M_\infty = 0.2$ and $M_\infty = 0.85$ and different α

Mesh	M_∞	α	ΔC_X	ΔC_Z	ΔC_{my}
Coarse	0.2	0	2.2	−14.6	−11.4
	0.2	10	−6.5	−4.2	−4.8
	0.2	20	9.1	−7.3	−1.3
Medium	0.2	0	1.4	−9.3	−7.2
	0.2	10	−4.3	−2.7	−3.0
	0.2	20	6.1	−4.5	−0.7
Fine	0.2	0	0.9	−5.8	−4.4
	0.2	10	−2.8	−1.7	−1.9
	0.2	20	3.4	−2	−0.4
Coarse	0.85	0	2.1	−17	−25
	0.85	5	1.2	−6.8	−8.9
	0.85	10	1.1	−4.5	−5.7
Medium	0.85	0	1.4	−11.5	−16.7
	0.85	5	0.74	−4.6	−5.7
	0.85	10	0.71	−2.9	−3.4
Fine	0.85	0	0.9	−7.4	−10.1
	0.85	5	0.5	−3.0	−3.6
	0.85	10	0.44	−1.8	−1.9

Δ is the difference with respect to the Richardson extrapolation value of C_X, C_Z, and C_{my}.

3.9 times higher with respect to the coarse mesh. Also in this case, the medium mesh is selected for the continuation of the study.

Figure 4 shows the medium mesh employed in this study for the subscale aircraft as an example. In particular, the left side of Fig. 4 features the distribution of the elements along the chord and span, as well as the limit of the inner block. The right side of the figure highlights a plane perpendicular to the aircraft span at the location of the mean aerodynamic chord.

The meshes described so far are used to study the effect of α, sideslip β, and control surface (elevator, aileron, and rudder) deflection on the forces and moments acting on the aircraft. The aircraft geometry is modified to take into account the control surface deflection. For simplicity, it is supposed that the control surfaces do not introduce gaps, i.e., they smoothly change the geometry. The accuracy of this hypothesis will be shown in Sec. III, where the simulations are compared to the experimental data. The mesh software employed allows the connection of the mesh to some points along the wing. Hence, it is possible to keep the same mesh for the aircraft with and without control surface deflection; only the inner layer is rotated to follow the aircraft geometry. The mesh described so far is mirrored with respect to the symmetry plane to simulate the sideslip angle effect, as well as the aileron and rudder effects.

III. Comparison of Numerical and Experimental Data

In this section, the various experimental and numerical methods are compared for the subscale aircraft geometry. First, Sec. III.A compares wind tunnel and flight tests to identify discrepancies between the two. Then, Sec. III compares the experimental data with various numerical methods, particularly the VLM, the panel method, and RANS simulations.

A. Comparison of Static Coefficients from Wind Tunnel and Flight Experiments

The aerodynamic coefficients identified from the flight tests are compared with the wind tunnel experiments in Figs. 5a and 5b. The force and moment coefficients are split into the two figures, allowing different scales and improving readability.

As introduced in Sec. II.A, the flight and wind tunnel models share the same geometry and dimensions. However, the wind tunnel model is only half of the flight model, so the effect of the missing aileron and rudder is assumed to be superposable.

The aerodynamic coefficients considered are only the static ones, without the sideslip effect, which could not be tested in the wind tunnel. As introduced in Sec. II.A.1, the aerodynamic coefficients of the flight model were identified in a previous study [15], and the error bars indicate the root mean square deviation.

For this comparison, α is limited between 0 and 15 deg, and the deflection of the control surfaces between ± 8 deg. Additionally, as will be discussed in Sec. III.C, the control surface authority depends on α. As the maneuvers in flight experiments are primarily conducted at $\alpha \approx 7.5$ deg, the coefficients shown here for the wind tunnel experiment are determined at the same angle of attack. The wind tunnel aerodynamic coefficients include the 95% confidence interval of the coefficient estimate. The impact of the angle of attack on the aerodynamic coefficients is discussed in Sec. III.C.

Figures 5a and 5b show that most of the coefficients predicted from the flight experiments are, in absolute value, higher than the ones obtained from the wind tunnel experiment. However, the most relevant coefficients of the three control surfaces, i.e., C_{mx,δ_a}, C_{my,δ_e}, and C_{mz,δ_r}, are quite close. The coefficients dependent on α show some discrepancies, but their values from the flight experiment are not as meaningful because α cannot be varied arbitrarily. Additionally, the flight test article incorporates the landing gear, the engine, and the pylon, which are not present in the wind tunnel experiment. This difference could, e.g., explain the difference in $C_{my,\alpha}$.

Based on the results presented here, for the continuation of the study, the static aerodynamic coefficients used to compare with the

Downloaded by Technische Universiteit Delft on November 12, 2026 | http://arc.aiaa.org | DOI: 10.2514/1.C038513

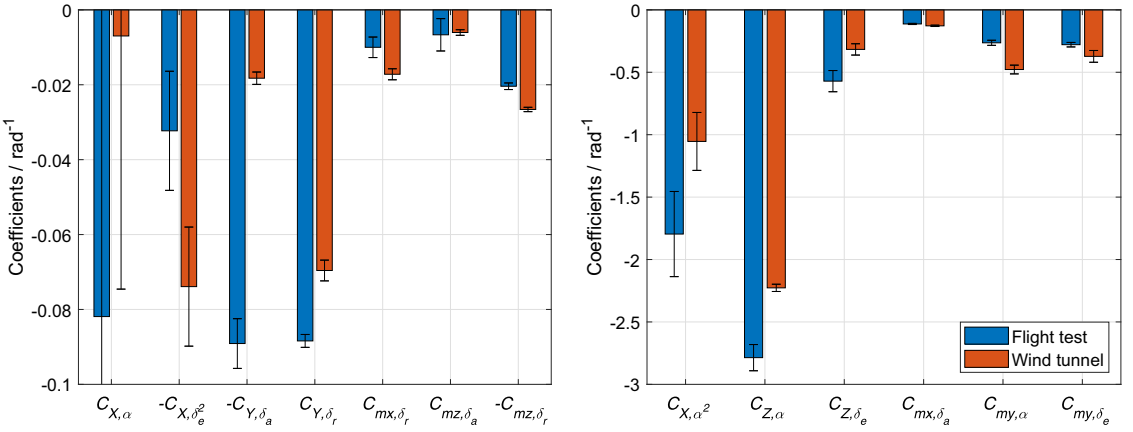


Fig. 5 Static aerodynamic coefficients from flight and wind tunnel experiments. The coefficients are grouped based on their value for easier readability.[§]

numerical simulations are extracted from the wind tunnel experiment because, as shown in Sec. III.C, the angle of attack impacts all aerodynamic coefficients.

B. Comparison of Aerodynamic Coefficients from Simulations and Experiments

The aerodynamic coefficients measured during flight and wind tunnel experiments are compared with various numerical methods, particularly the VLM, the panel method, and a numerical method based on the RANS equations. As discussed in Sec. II.A, the static experimental coefficients are extracted from wind tunnel data, excluding the ones depending on β. The dynamic coefficients depending on $\hat{p}$, $\hat{q}$, and $\hat{r}$ are extracted from the flight experiments. The VLM and panel methods feature both static and dynamic coefficients. Conversely, RANS simulations are employed only for the static coefficients. The coefficients are estimated with a fixed $\alpha = 7.5$ deg for better comparison with the flight experiment. The effect of α is further investigated in Sec. III.C.

Figure 6 summarizes the aerodynamic coefficients obtained using the different methods. The force and moment coefficients are divided into five figures, allowing different scales and improving readability. The coefficients obtained numerically are obtained by linear interpolation, as, e.g., $C_{Z,\alpha}$ is obtained by fitting a linear curve between α and C_Z. Additionally, each coefficient also features the 95% confidence interval of the coefficient estimate. Large error bars indicate lower linearity between the force or moment and the variable that induces it. The forces and moments induced by each variable, and hence the coefficients depicted in Fig. 6, are now analyzed separately in order to assess how the different numerical methods compare with the experimental data.

The analysis starts with the derivatives of C_X, C_Z, and C_{my} with respect to α, as shown in Figs. 6a–6e. It can be seen that the coefficients predicted by RANS simulations are always within the experimental error bars, i.e., the error bars of the simulation and the experiment overlap. Conversely, the VLM and panel methods consistently predict higher coefficients with respect to the measured values. The only case in which they fall within the experimental error bars is for $C_{X,\alpha}$ (Fig. 6e), which has a high uncertainty compared to the mean value.

Regarding the coefficients related to β depicted in Figs. 6b–6e, also in this case the coefficients predicted by RANS simulations are closer to and within the error bars with respect to the experimental data. However, there is a significant difference for $C_{Y,\beta}$ (Fig. 6b), for which the predicted value from RANS is half the experimental one. However, as discussed before, $C_{Y,\beta}$ is derived from flight experiments in which the engine and the landing gear are present, which are not present in the simulation. The VLM and panel methods predict an even lower $C_{Y,\beta}$ than RANS. Regarding $-C_{mx,\beta}$ and $C_{mz,\beta}$ (Fig. 6e), the VLM predicts higher derivatives, and the panel method predicts lower derivatives compared to the experiments. However, the two methods show a much better prediction of $C_{mz,\beta}$.

Next, the dynamic coefficients, i.e., the coefficients due to the roll rates, are analyzed. The dynamic coefficients from RANS simulations are calculated using a rotating reference frame with $\hat{p} = \hat{r} = 0.0013,\ 0.0065,\ 0.013$ and $\hat{q} = 0.004,\ 0.02,\ 0.04$. The rotating frame is imposed on the standard far-field boundary conditions.

There are significant differences between the simulations and the experiments for some coefficients. For example, $C_{Z,q}$ in Fig. 6a is more doubled in the simulations than in the experiment, with the VLM being closer. $C_{my,q}$ in Fig. 6a predicted by the VLM and panel method falls within the experimental error bars, while RANS strongly underpredicts it. The simulation methods predict a $C_{mx,p}$ in Fig. 6b that is slightly higher than the experimental value, with the VLM being closer. However, they overpredict $C_{mz,p}$ by more than a factor of three, as can be seen in Fig. 6d. Finally, $C_{Y,r}$ (Fig. 6c) in the experiment is more than twice that of the VLM and RANS simulations and even more for the panel method, with RANS being closer to the experiment. The VLM simulations closely resemble $C_{mx,r}$ in Fig. 6c, whereas the RANS simulations and panel method strongly underpredict it, particularly the latter. In contrast, the panel method closely predicts the experimental $C_{mz,r}$ in Fig. 6d, while the VLM and RANS underpredict it, particularly the latter. Overall, the coefficients predicted by the VLM are closest to the experimental data, followed by the panel method and the RANS simulations. In particular, the VLM simulations are closer to the experimental coefficients than the panel method in 57% of the cases. Similarly, the panel method is closer to the experimental data than the RANS simulations in 57% of the coefficients.

The forces and moments due to the aileron, elevator, and rudder are simulated with the three numerical methods. Starting with the elevator in Fig. 6b, C_{Z,δ_e} and C_{my,δ_e} are closely predicted by the RANS simulations; differently, both the VLM and panel method overestimate them. The VLM and panel methods also overpredict the effect of the aileron on C_Y, C_{mx}, and C_{mz} with respect to the experimental data in Figs. 6c–6e. The RANS simulations correctly predict C_{Y,δ_a} (Fig. 6c), but they underpredict C_{mx,δ_a} and C_{mz,δ_a} in Figs. 6c and 6d. Now focusing on the rudder, the VLM and panel method simulations overpredict C_{Y,δ_r} and C_{mz,δ_r} in Figs. 6d and 6e; differently, the RANS simulations underpredict both of them, particularly the former. All three numerical methods slightly underpredict C_{mx,δ_r} with respect to the experimental data in Fig. 6e.

Some of the discrepancies in control authority predicted by the numerical methods are related to the tested conditions. In particular, as introduced before, it was supposed that the flight tests are conducted at $\alpha \approx 7.5$ deg, and accordingly the other coefficients are also calculated for the same angle of attack. However, as will be

[§]Note: Derivatives are determined with respect to $\alpha \approx 7.5$ deg.

Downloaded by Technische Universiteit Delft on November 12, 2026 | http://arc.aiaa.org | DOI: 10.2514/1.C038513

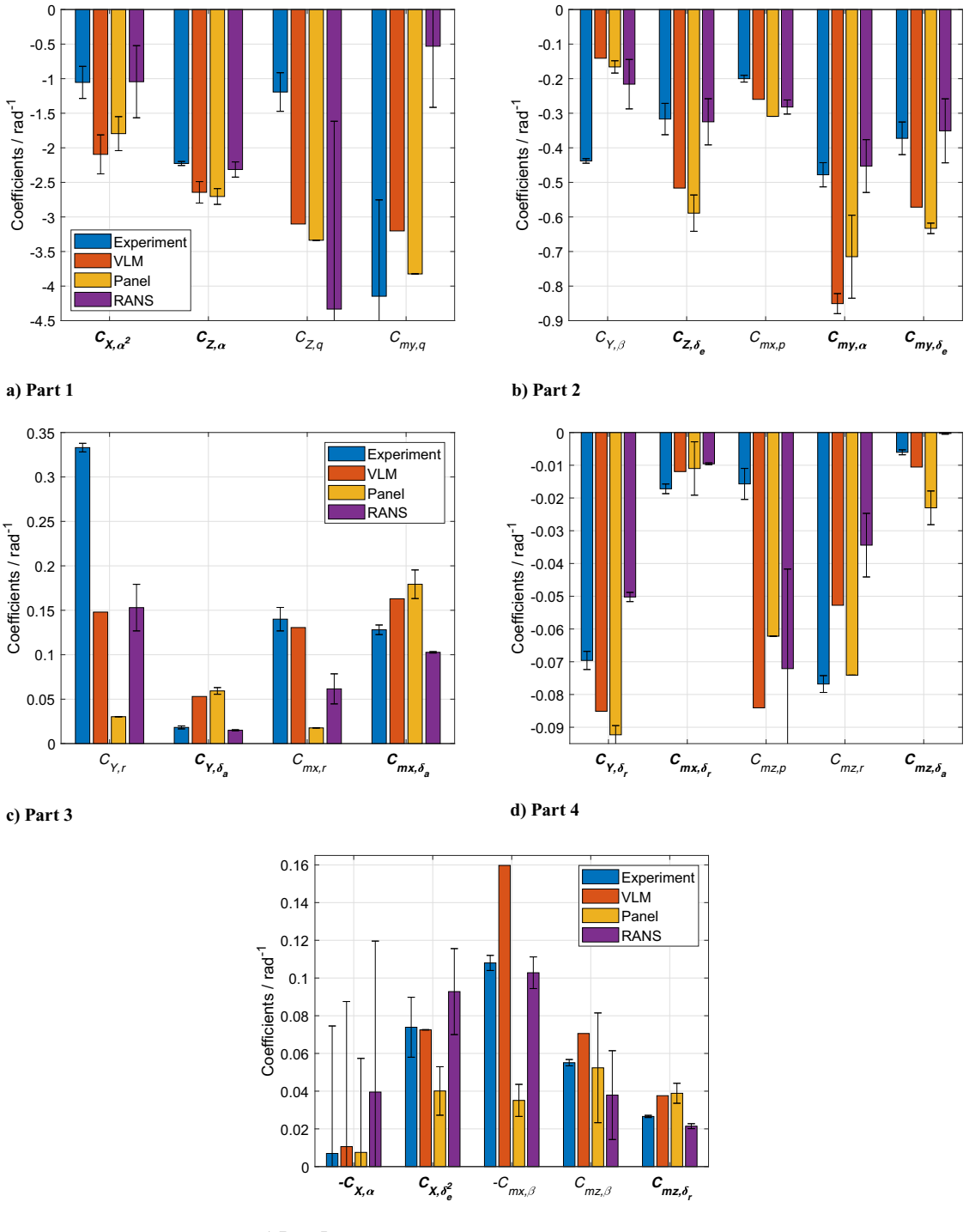


Fig. 6 Comparison of experimental and numerical aerodynamic coefficients. Bold coefficients indicate experimental data extracted from wind tunnel experiments; the remaining ones are from flight tests[¶].

discussed in Sec. III.C, the coefficients are angle-of-attack dependent, and the difference between simulations and experiments also depends on α. Additionally, when considering the control effectiveness predicted by RANS simulations, it should be considered, as introduced in Sec. II.B.3, that for easier mesh creation, the control surfaces do not introduce any gap in the geometry. The gaps introduced by a control surface can induce 3D flow, which could enhance the control effectiveness, particularly in the trailing-edge area where crossflow is present. Further analyses are underway to obtain a more in-depth comparison between the different methods, e.g., by comparing the pressure distribution along the model.

Overall, the comparison shows that the static aerodynamic coefficients predicted with RANS simulations are always the closest to the experimental data, being, in most cases, inside the error bars. Considering both static and dynamic coefficients, the VLM and panel method simulations show similar coefficients for approximately half of them. The VLM results are closer to the experimental data; in particular, 60% of the coefficients are closer to the experiment than those from the panel method. Regarding the dynamic coefficients, the VLM is closer to the experimental data with respect to the panel method and RANS; however, for some coefficients, the

[¶]Note: Derivatives are determined with respect to $\alpha \approx 7.5$ deg. The coefficients are grouped based on their values for easier readability.

Downloaded by Technische Universiteit Delft on November 12, 2026 | http://arc.aiaa.org | DOI: 10.2514/1.C038513

differences are consistent. How to account for these differences is discussed in Sec. IV.

The next section (Sec. III.C) analyzes the effect of the angle of attack on the aerodynamic coefficients by comparing wind tunnel data with RANS and VLM simulations.

C. Subscale Aircraft Performance with Angle of Attack

The analysis conducted so far has considered a fixed angle of attack α supposed to lie in the region of a linear relationship between α and the forces and moments acting on the aircraft, and consequently it has been supposed that the effects of the other coefficients are superposable, i.e., the coefficients are independent of α. However, the superposition effect may not hold true, particularly at high α. This section investigates the possible presence of nonlinearities by employing RANS simulations and comparing them with experiments.

Figures 7a and 7b show the relationship between drag C_D and pitching moment C_{my} coefficients as functions of the lift coefficient C_L, respectively. The force and moment coefficients are calculated using wind tunnel measurements and RANS simulations. The experimental force and moment coefficients include the 95% confidence interval of the sum of the systematic and random uncertainties.

Figure 7b clearly highlights a nonlinearity, herein defined as a *pitch break*, i.e., the switching from $C_{my,\alpha} < 0$ to $C_{my,\alpha} > 0$. Overall, the RANS simulations are able to predict the same trend as the wind tunnel experiment. Higher discrepancies can be noticed at $C_L \geq 0.6$ when the pitch break occurs. However, the slight discrepancies could be related to the different treatment of the boundary layer. In particular, the boundary layer in the wind tunnel model is not tripped in the inner wing; however, in the RANS simulations, the flow is assumed to be fully turbulent.

The source of the pitch break has been discussed in [18], where it has been shown that already at low α, crossflow occurs in the trailing-edge area of the inner wing, which extends to the outer wing at higher α. The pitch break starts occurring when the inner wing contributes more than the outer wing to the total C_Z and hence induces a positive contribution to the pitching moment, leading to $C_{my,\alpha} > 0$.

As the change in α strongly impacts the flow on the outer wing, where the control surfaces are located, a change in the control surfaces' control authority is also expected. Figures 8a–8c show the impact of α on C_{mx,δ_a}, C_{my,δ_e}, and C_{mz,δ_r}, respectively. Each figure features wind tunnel experiment data and results from simulations conducted with the VLM and RANS. Furthermore, the figures include the coefficients from the flight tests used in Sec. III, where it was supposed that the flight tests are, on average, conducted at $\alpha \approx 7.5$ deg. The experiments and simulations are conducted at $\alpha \leq 20$ deg, i.e., before the occurrence of the pitch break. Both the wind tunnel experiments and the RANS simulations include the 95% confidence interval of the coefficient estimate.

Because of the crossflow in the trailing-edge area of the outer wing, where the control surfaces are located, as seen both experimentally [14] and numerically [18], the control authority of all control surfaces decreases with α. For the wind tunnel experiment, C_{mx,δ_a} and C_{my,δ_e} slightly increase in absolute value; however, this effect is not present in either the VLM or RANS simulations. This behavior is unclear and could be related to the laminar flow in the inner wing, which leads to a different evolution of the flow on the wing, as discussed earlier for the pitching moment. The most evident change with α occurs with C_{mz,δ_r}, for which the control authority is more than halved between $\alpha = 0$ deg and $\alpha = 20$ deg. Figure 8d shows the impact of α on $C_{mz,\beta}$; in this case, wind tunnel data are not available because only a half model is tested. The VLM predicts an increase in the coefficient with α, whereas the RANS predicts a slight decrease between $\alpha = 0$ deg and $\alpha = 10$ deg, followed by an increase. It should be noted how the relatively large winglet (Fig. 3b) of the subscale aircraft, with respect to the full-scale aircraft considered in Fig. 8d, strongly impacts the effect of the sideslip angle β. However, VLM simulations, not included here for brevity, indicate a directionally stable aircraft even without winglets.

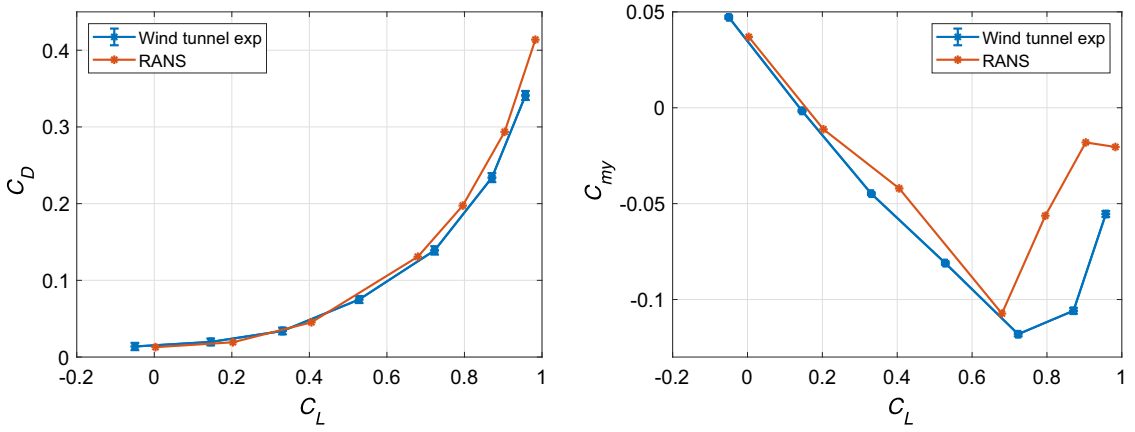
As discussed for the other coefficients in Sec. III, the RANS simulations closely resemble the experimental data. The VLM can predict the trend of the change occurring with α. However, the predicted coefficients are up to 50% larger in absolute value with respect to the experimental data. The VLM is not suited to predict the crossflow and vortical structures that occur on the aircraft at higher α; however, even at low α, the coefficients predicted by the VLM are consistently relatively higher than those from the other two methods.

Overall, this section has shown how the aerodynamic coefficients depend on α, even at α lower than at the occurrence of the pitch break. However, the pitch break occurrence in terms of α, and hence of the flow on the aircraft, depends on the Mach number M_∞, as will be shown in the next section (Sec. IV) when considering the full-scale aircraft.

D. Superposition of the Moments from Control Surface Deflection

The control surface located in the trailing-edge area of the outer wing, and considered so far as one acting surface, is divided into three elements as depicted in Fig. 9a, labeled CS1, CS2, and CS3 from the inner to the outer wing.

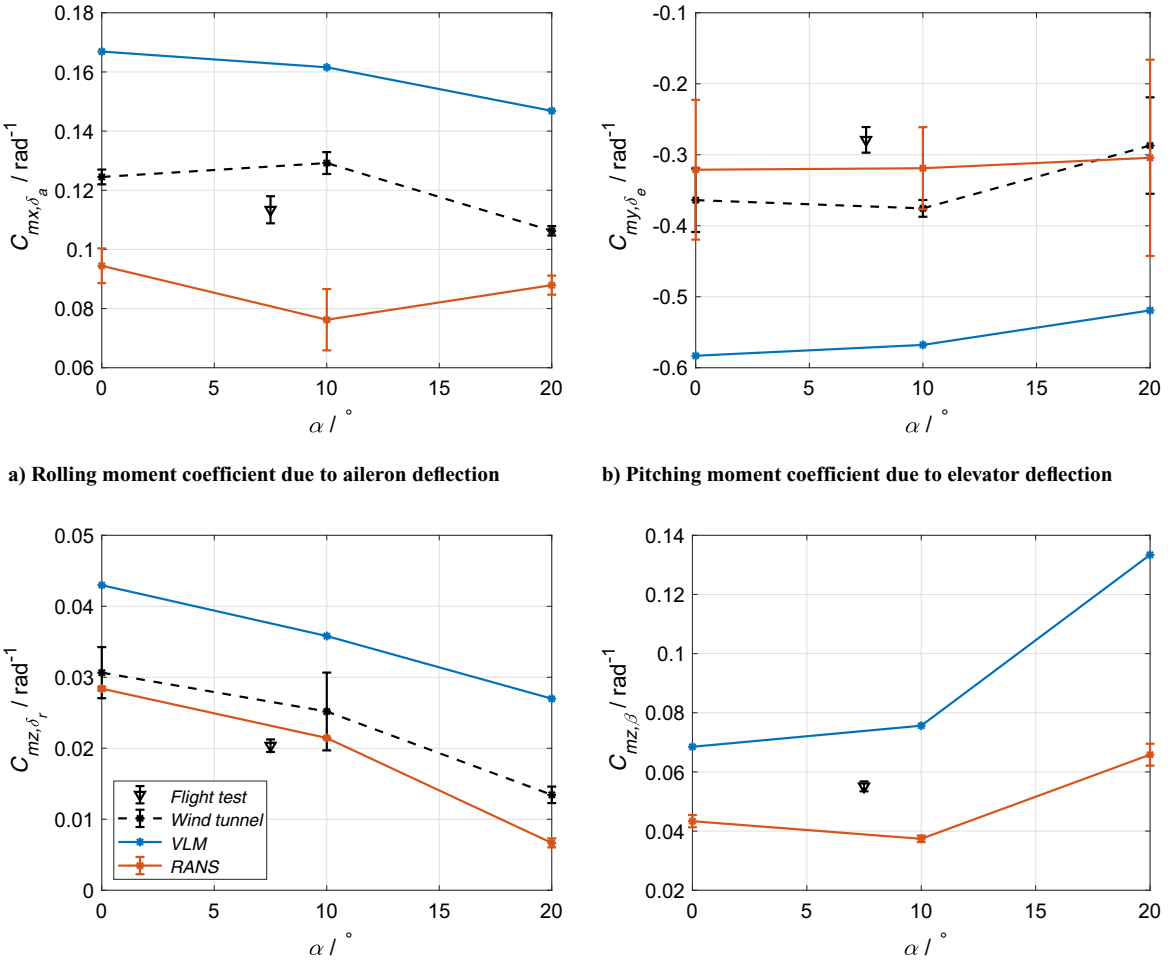
Figure 9b shows the pitching moment generated by the individual surfaces, $C_{my,\delta_{e_i}}$ with respect to the pitching moment generated when the three surfaces are used as one, C_{my,δ_e}, at various α. The sum of the three contributions leads to 1.07, 1.02, and 1.07 at $\alpha = 0$, 10, and 20 deg, respectively. However, these differences fall within the 95% confidence interval of the coefficient estimate, included in the figure as error bars. Note that δ_e tested here varies between ± 16 deg. At higher deflections, the superposition effect could be less accurate. Furthermore, Fig. 9b shows that the pitching moment



a) Drag coefficient for subscale aircraft **b) Pitching moment coefficient for subscale aircraft**

Fig. 7 Impact of α on C_D and C_{my} for subscale aircraft at $M_\infty = 0.07$ and $Re_{\bar{c}} = 1.3 \cdot 10^6$.

Downloaded by Technische Universiteit Delft on November 12, 2026 | http://arc.aiaa.org | DOI: 10.2514/1.C038513



a) Rolling moment coefficient due to aileron deflection

b) Pitching moment coefficient due to elevator deflection

c) Yawing moment coefficient due to rudder deflection

d) Yawing moment coefficient due to sideslip angle

Fig. 8 Impact of α on C_{mx,δ_a}, C_{my,δ_e}, and C_{mz,δ_r} for subscale aircraft at $M_\infty = 0.07$ and $Re_{\bar{c}} = 1.3 \cdot 10^6$.

created decreases when moving outboard, for which the CS size also decreases. With increasing angle of attack, the contribution of CS1 increases, whereas the contributions of CS2 and CS3 slightly decrease.

In Fig. 9c, a similar analysis is conducted when considering the control surfaces acting as an aileron, i.e., in their ability to modify C_{mx}. In this case, the higher contribution comes from the outer surface. With increasing α, CS3 tends to increase its contribution, CS2 decreases, and the contribution of CS1 remains almost constant. The ratio between the sum of the moment created by the three surfaces and the moment created by the three surfaces when used as one amounts to 1, 1.01, and 0.97, for $\alpha = 0$, 10, and 20 deg, respectively.

Finally, Fig. 9d shows the C_{mz} created by the rudder, with elevator deflection varying between ± 16 deg with steps of 8 deg. In this case, the three surfaces are employed as one. The comparison shows that the effect of the elevator deflection does not significantly impact the rudder.

Based on this analysis, it can be concluded that the effect on the rolling, pitching, and yawing moments of each deflected control surface is independent of the deflection of another control surface. Therefore, the superposition principle can be applied when predicting the combined effect of deploying multiple control surfaces at once. This conclusion is valid for at least the deflection angles and α tested here.

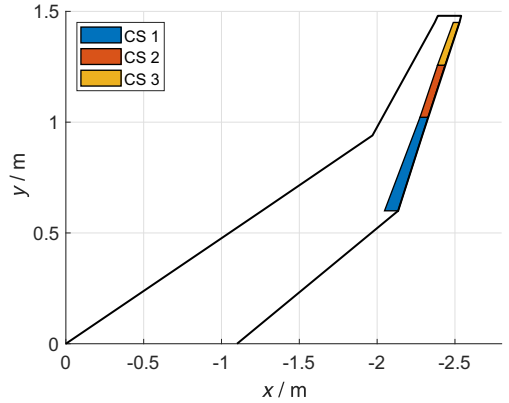
IV. Synthesis of Full-Scale Aerodynamic Model

The aerodynamic model for the full-scale aircraft is derived by combining different tools, based on the comparison conducted so far with the subscale aircraft (Sec. III). It should be noted that the geometry of the full-scale aircraft is slightly different with respect to the subscale aircraft and that the dimensions and types of control surfaces considered also partly vary.

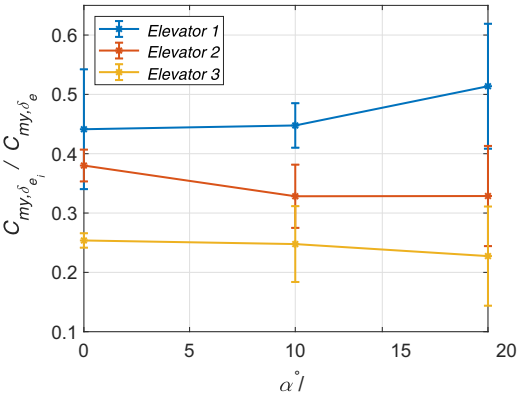
The approach pursued here is to use the numerical methods that most closely predict the experimental data, as discussed in Sec. III. The RANS simulations more closely predict the experimental aerodynamic coefficients, and, as shown in Sec. III.C, they can predict nonlinear effects such as the impact of α on C_{my} or on the control authority of the control surfaces. For this reason, RANS simulations are employed to derive most of the force and moment derivatives required to describe the aircraft; however, it should be considered that the computational effort and the level of geometric detail needed for the RANS simulations are significantly higher than for the other methods. In particular, RANS simulations are used to calculate the effects of the angle of attack α, the sideslip angle β, and of the deflections due to elevator δ_e, aileron δ_a, and rudder δ_r. The RANS simulations are also used to estimate the impact of control surfaces not tested in the subscale aircraft, such as a high-lift flap (δ_f) and a droop nose or leading-edge flap (δ_d).

Section III has also shown that VLM simulations can better predict the dynamic coefficients with respect to the panel method and RANS simulations. However, because some of the coefficients show large discrepancies with respect to the experimental values, the coefficients determined with the VLM are calibrated with experimental data. Basically, it is supposed that the offset in the VLM results is the same also for the full-scale aircraft. Hence, VLM simulations are used to determine the dynamic force and moment derivatives due to $\hat{p}$, $\hat{q}$, and $\hat{r}$. Regarding the calibration procedure,

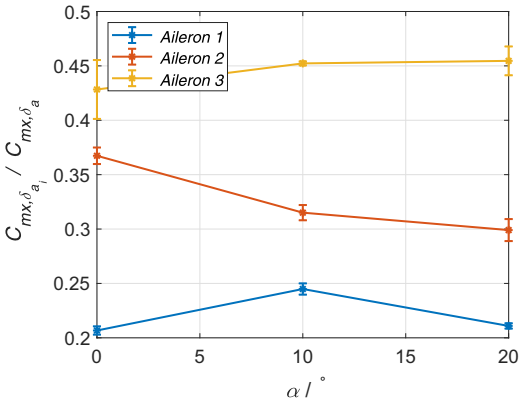
Downloaded by Technische Universiteit Delft on November 12, 2026 | http://arc.aiaa.org | DOI: 10.2514/1.C038513



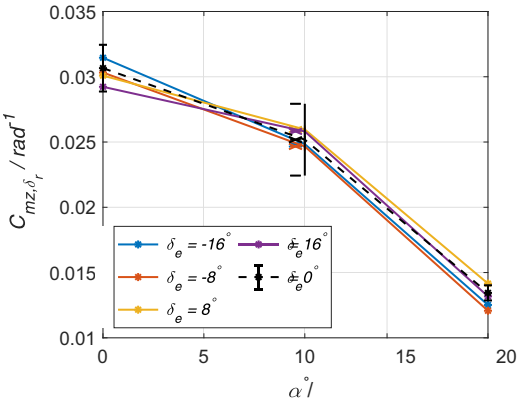
a) Split control surfaces on the trailing edge



b) Contribution of the individual CS to the total pitching moment coefficient due to the elevator at different α



c) Contribution of the individual CS to the total rolling moment coefficient due to the aileron at different α. The anti-symmetric deflection on eitherwing half is considered



d) Superposition of elevator and rudder effects

Fig. 9 Wind tunnel measured effect of superposition of control surfaces' control authority for subscale aircraft at $M_\infty = 0.07$ and $Re_{\bar{c}} = 1.3 \cdot 10^6$.

Table 7 Force and moment coefficient dependencies (marked "R" when determined with RANS simulations and "CV" VLM simulations calibrated with experiments)

Coefficient	α	$\beta(\alpha)$	$\hat{p}(\alpha)$	$\hat{q}(\alpha)$	$\hat{r}(\alpha)$	$\delta_e(\alpha)$	$\delta_a(\alpha)$	$\delta_r(\alpha)$	$\delta_f(\alpha)$	$\delta_d(\alpha)$
C_X	R					R	R	R	R	R
C_Y		R			CV		R	R		
C_Z	R			CV		R			R	R
C_{mx}		R	CV		CV		R	R		
C_{my}	R			CV		R			R	R
C_{mz}		R	CV		CV		R	R		

the coefficients shown in Sec. III are used to determine a calibration factor, as, e.g., $C_{Z,q_{\text{exp}}}/C_{Z,q_{\text{vlm}}}$. This factor is then used to scale the $C_{Z,q}$ coefficient calculated for the full-scale aircraft with the VLM. The trend of the derivatives as a function of M_∞ and α is dictated by the VLM simulation, but the curves are scaled with the calibration factor. An example is presented later in this section.

Table 7 indicates the dependencies of each force and moment, and they are marked with "R" if RANS simulations are employed and "CV" if VLM simulations calibrated with experiments are used. Furthermore, each coefficient is determined at different angles of attack α. The VLM simulations are also employed at transonic conditions. The suitability of this choice is discussed later in this section, where some results are presented.

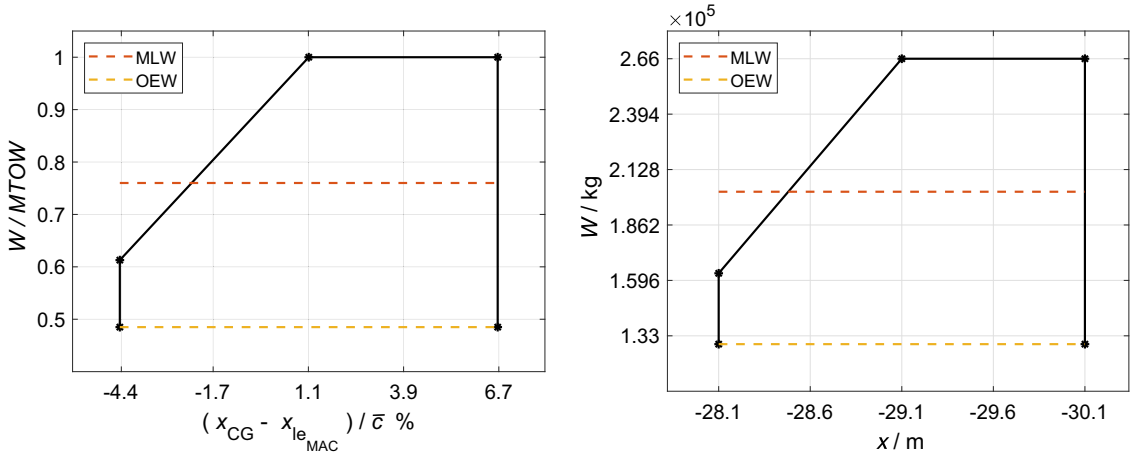
The simulations are conducted at the flight conditions listed in Table 8. The cases are intended to describe different flight phases, i.e., takeoff/landing, climb/descent, and cruise.

Table 8 Flight conditions

Parameter	h, m	M_∞	ρ_∞, kg/m^3	U_∞, m/s	Re_c, $\times 10^7$
	0	0.2	1.22	68.6	8.4
Takeoff/landing	0	0.25	1.22	85.1	10.5
	0	0.3	1.22	102.1	12.6
	5,450	0.4	0.70	127.5	10
Climb/descend	7,650	0.6	0.55	185.7	11.9
	9,750	0.7	0.43	210.4	11
Cruise	11,225	0.85	0.35	250.8	11.1

For each flight condition, the aerodynamic model is derived at different center-of-gravity (CG) values. The combinations of weight and CG range are shown in Fig. 10, where both the dimensional and dimensionless values are depicted in Figs. 10a and 10b, respectively.

Downloaded by Technische Universiteit Delft on November 12, 2026 | http://arc.aiaa.org | DOI: 10.2514/1.C038513



a) Dimensionless CG range and weight **b) Dimensional CG range and weight**

Fig. 10 Dimensionless and dimensional center of gravity (CG) and aircraft weight with $\bar{c} = 18$ m.

Downloaded by Technische Universiteit Delft on November 12, 2026 | http://arc.aiaa.org | DOI: 10.2514/1.C038513

The weights considered in this study are related to the FV-1000 [12], with a maximum takeoff weight (MTOW) of $266 \cdot 10^3$ kg. The maximum landing weight (MLW) is supposed to be 76% of the MTOW.

In Fig. 10b, the CG excursion is shown with respect to the leading-edge location of the mean aerodynamic chord, where $\bar{c} = 18$ m, with $S = 898$ m^2 and $b = 65$ m. The weights are divided with the MTOW. The most rearward CG position of 30.1 m (from the aircraft nose) is located 0.5 m upstream of the neutral point. The maximum CG excursion is 2.0 m and can be supported up to 61% of the maximum takeoff mass. At the maximum takeoff mass, the CG excursion is limited to 1.0 m [13]. The moment coefficients shown hereafter are calculated with respect to the most forward CG at MTOW, i.e., $x_{CG} = -29.1$ m. In the subsequent paragraphs, the aerodynamic model is highlighted.

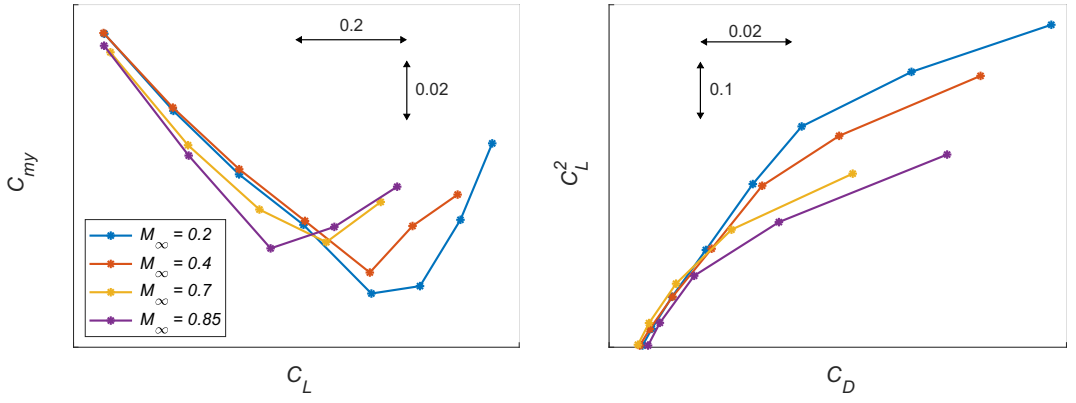
Figure 11 shows the impact of the angle of attack α on C_L, C_D, and C_{my}, calculated with RANS simulations. C_{my} is shown as a function of C_L, and C_L^2 as a function of C_D in Figs. 11a and 11b, respectively.

Starting from Fig. 11a, it is evident that the pitch break occurs at lower C_L, with increasing M_∞. A similar trend has been observed in previous studies about flying wings [19]. It should be considered that the occurrence of the pitch break also depends on the engine location [20] and on its effect on the flow, which are not considered in this work. In Fig. 11b, it can be observed that at the same C_L at which the pitch break starts, a clear change in slope is visible in $C_D - C_L^2$. The flow on the outer wing tends to separate at higher α, leading to an increase in the drag coefficient and a reduction in the nose-down pitching moment, leading to the occurrence of the pitch break [18].

The pitch break limits the usable maximum lift coefficient. However, as shown in [21], it is possible, with adequate sizing of the control surfaces, to trim the aircraft at the considered operating conditions and perform maneuvers. However, disturbances from the initial trim condition at different flight phases, which, e.g., could be induced by gusts, could lead to an increase in α such that $C_{my,\alpha} > 0$. For this reason, it could be required to have an angle-of-attack limiter on the aircraft. Alternatively, it is possible to postpone the occurrence of the pitch break to higher C_L by redesigning the airfoil sections while keeping the planform fixed [22], or by adding flow control devices such as vortex generators [23].

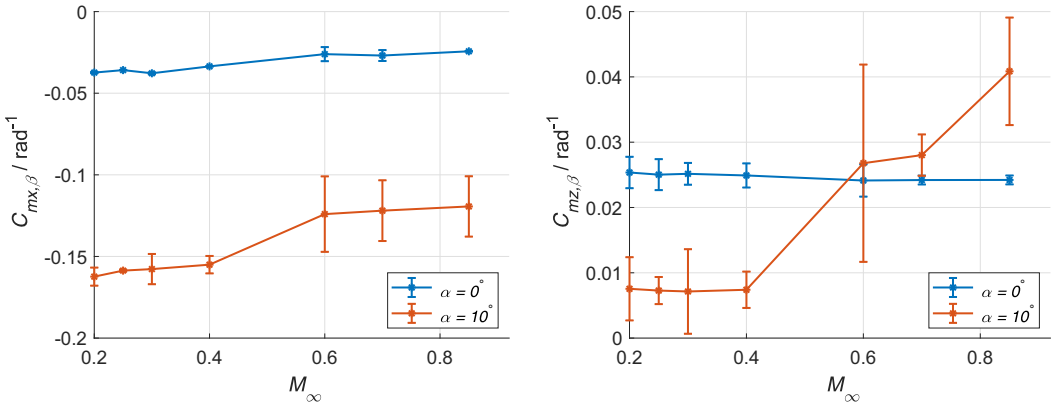
The effects of the angle of attack α and the Mach number M_∞ are now considered for different aerodynamic coefficients. The figures presented herein include, as error bars, the 95% confidence interval of the coefficient estimate. A high confidence interval indicates lower linearity between the moments and the variable that induces them. For this reason, the aerodynamic model is used as a look-up table. However, it is preferred to estimate the coefficients to highlight some general trends here.

Figures 12a and 12b show the impact of α and M_∞ on $C_{mx,\beta}$ and $C_{mz,\beta}$, respectively. The sideslip angles considered are $\beta = 7.5$ deg and 15 deg. The results highlight a laterally stable ($C_{mx,\beta} < 0$) and directionally stable ($C_{mz,\beta} > 0$) aircraft in the simulated ranges of α and M_∞. The results clearly indicate that the effect of β is dependent on α. A similar trend was observed in Sec. III.C; however, because the occurrence of crossflow and vortices, and hence of the pitch break, varies with α at different M_∞, the moment derivatives with sideslip also depend on the Mach number. The reason for this is clear by observing the evolutions of the stability derivatives in Figs. 12a and 12b as a function of M_∞. The derivatives are almost constant for $M_\infty \leq 0.4$. For $M_\infty > 0.4$, there is little change in the derivatives at zero angle of attack. However, for $\alpha = 10$ deg, a large



a) Pitching moment coefficient **b) Drag coefficient**

Fig. 11 RANS-predicted effect of α on C_L, C_D, and C_{my} at different operating conditions.



a) Rolling moment due to sideslip **b) Yawing moment due to sideslip**

Fig. 12 RANS-predicted effect of Mach number on rolling and yawing moment coefficients at two angles of attack.

Downloaded by Technische Universiteit Delft on November 12, 2026 | http://arc.aiaa.org | DOI: 10.2514/1.C038513

change can be observed. Both the rolling moment due to sideslip and the yawing moment due to sideslip increase with Mach number. The formation of shocks at these flight conditions leads to a different development of the vortical structures occurring at $\alpha = 10$ deg on the left- and right-hand sides of the aircraft, leading to the observed changes in the moment coefficients.

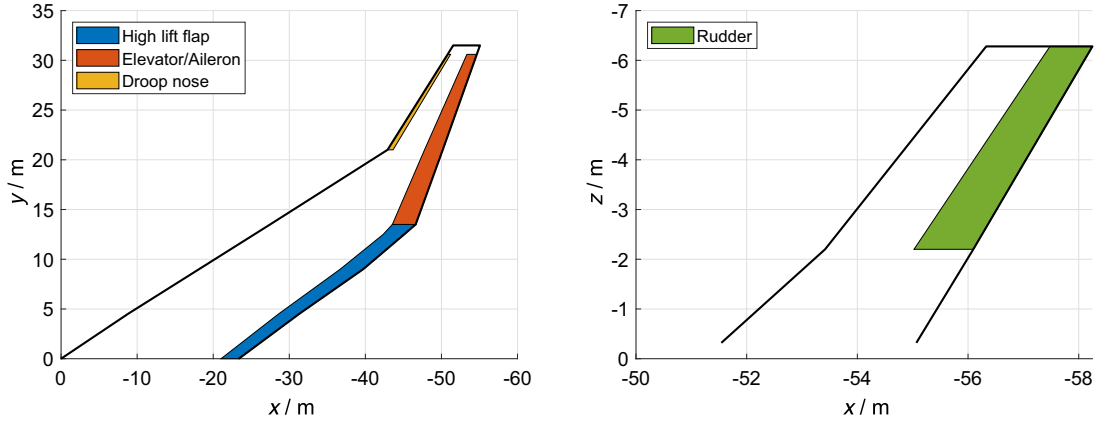
For all flight conditions considered, the asymmetry in the flow developing on the left and right wings leads to a slight reduction of C_L acting on the aircraft, amounting to approximately 8% at $\alpha = 10$ deg and $\beta = 15$ deg. It should be noted that the certification requirement specifies a maximum crossflow speed of 30 knots, which at $M_\infty = 0.2$ corresponds to $\beta = 13$ deg and at $M_\infty = 0.85$ corresponds to $\beta = 6$ deg [21].

The effects of α and M_∞ on the control surfaces' control authority are now investigated. Figure 13 depicts the control surfaces simulated with RANS simulations. In particular, Fig. 13a shows a control surface on the inner wing, which acts as a high-lift flap; the control surface on the trailing edge of the outer wing, which is used as an elevator and as an aileron; and a droop nose on the leading edge of the outer wing. Figure 13b shows the rudder on the winglet. The simulations with the aileron and rudder are conducted by mirroring the geometry with respect to the symmetry plane. The control surfaces depicted here are not intended to be the final ones to be implemented on the aircraft. In particular, the high-lift flap and the droop nose were not considered in Sec. III. They are tested here to evaluate their ability to increase the usable maximum C_L, as required at the lowest tested speed ($M_\infty = 0.2$) to satisfy the certification requirements [21].

The effects of M_∞ and α on C_{mx,δ_a}, C_{my,δ_e}, and C_{mz,δ_r} are shown in Figs. 14a–14c, respectively. The control surface deflections used to calculate the coefficients are $\delta_a = \delta_r = -30$ deg :15 deg :30 deg and $\delta_e = -30$ deg :15 deg :0 deg. For the rudder, the surfaces on the left and right sides of the wing are deflected at the same angle; for the aileron, one side is deflected upward and the other side downward by the same angle. The figures include, as error bars, the 95% confidence interval of the coefficient estimate.

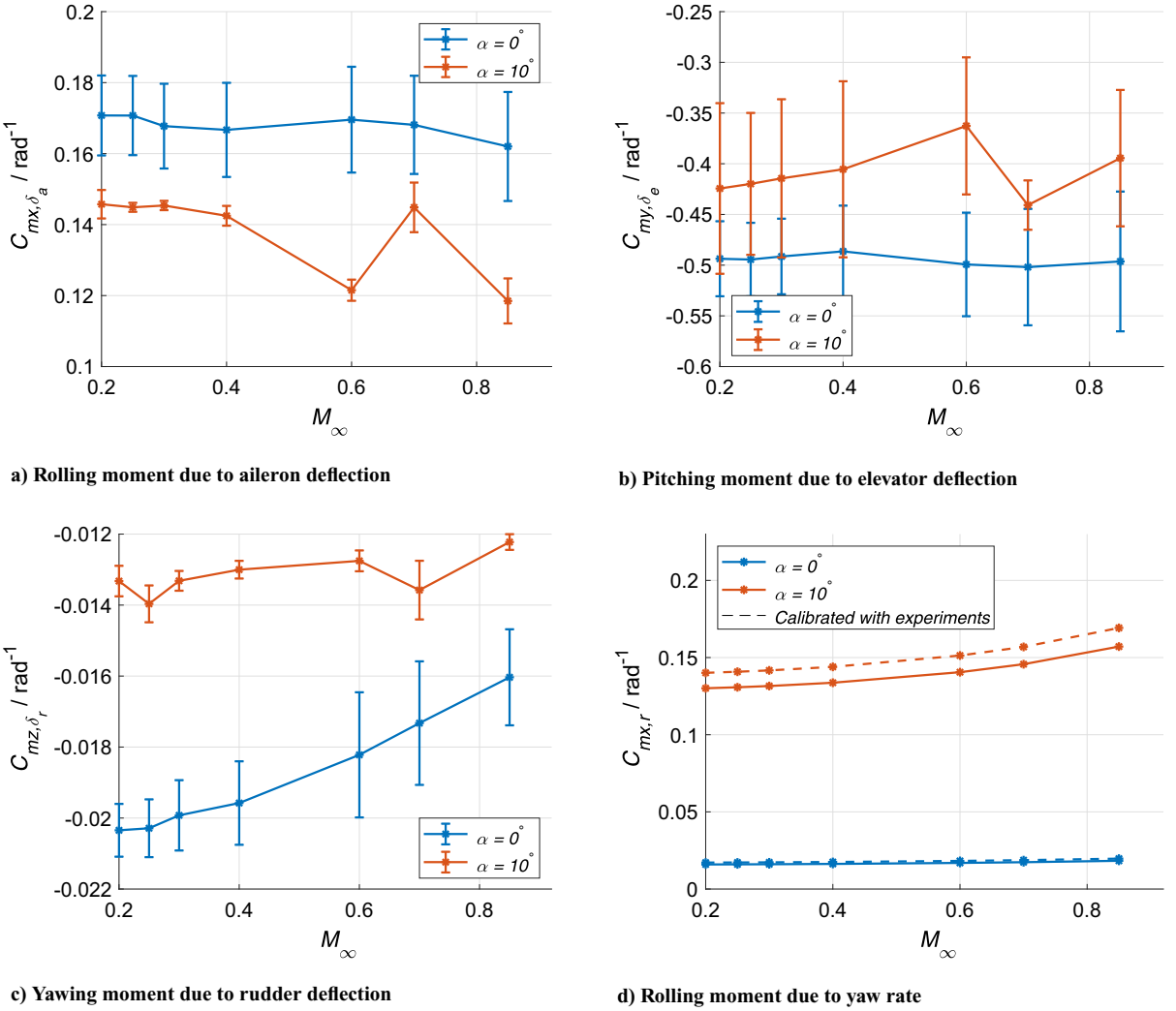
In Fig. 14a, the aileron effectiveness (C_{mx,δ_a}) tends to decrease with α. At $\alpha = 10$ deg, there is a nonlinear dependence of the control authority on Mach numbers for $M_\infty \geq 0.6$. In particular, between $M_\infty = 0.6$ and 0.7, C_{mx,δ_a} increases and then decreases again. This nonlinearity is related to the presence of a shock on the outer wing, which influences the flow downstream of it, particularly through interaction with the vortices developing on the outer wing, discussed in detail in [18]. Similar nonlinearities are visible in the relationship between Mach number and the control authority of the other control surfaces. Figure 12a showed that the rolling moment due to sideslip ($C_{mx,\beta}$) increases with α. Hence, high aileron deflections may be required to compensate for the sideslip-induced rolling moment in a gusty environment. However, it should be considered that an $\alpha = 10$ deg is an extreme case at transonic conditions, even when considering the longest $1 - \cos$ gust prescribed by certification documentation [24].

In Fig. 14b, the elevator effectiveness reduces with increasing angle of attack. For $\alpha = 0$ deg, the elevator effectiveness is relatively constant with the Mach number. Conversely, for $\alpha = 10$ deg, the elevator effectiveness decreases for $M_\infty \leq 0.6$, being higher at transonic cases.



a) High lift flap, aileron/elevator and droop nose on the wing **b) Rudder on the winglet**

Fig. 13 Full-scale aircraft and control surfaces simulated with RANS. Note: the aircraft geometry is not the same as the subscale, and the control surface dimension and distribution do not reflect the final layout.



a) Rolling moment due to aileron deflection

b) Pitching moment due to elevator deflection

c) Yawing moment due to rudder deflection

d) Rolling moment due to yaw rate

Fig. 14 RANS-predicted effect of M_∞ on the moment derivatives C_{mx,δ_a}, C_{my,δ_e}, C_{mz,δ_r}, and $C_{mx,r}$ due to aileron, elevator, rudder, and $\hat{r}$, respectively.

Considering the rudder mounted on the two winglets, Fig. 14c shows that the control authority of the rudders C_{mz,δ_r} significantly decreases with α. In general, the rudder effectiveness also decreases with M_∞. However, the decrease is higher at $\alpha = 0$ deg than at 10 deg, leading to a smaller decrease of the control authority of the rudder at a higher speed.

Figure 14d depicts the evolution of the rolling moment due to yaw rate ($C_{mx,r}$), showing an increase, in an absolute sense, with M_∞, dictated by the Prandtl–Glauert correction and a significant increase with α. The VLM code should not be able to predict the dynamic derivative at α for which separation occurs [7]. However, as observed in Sec. III.C, the VLM could predict the change but not the absolute value of the aerodynamic coefficients as a function of α before the occurrence of the pitch break. Hence, the VLM results are calibrated with the dynamic coefficients obtained from the flight tests, as explained at the beginning of this section. In this case, $C_{mx,r}$ slightly increases due to the calibration. For other dynamic derivatives the impact of the calibration factor is higher, e.g., for $C_{mz,r}$ the values are multiplied by 1.45.

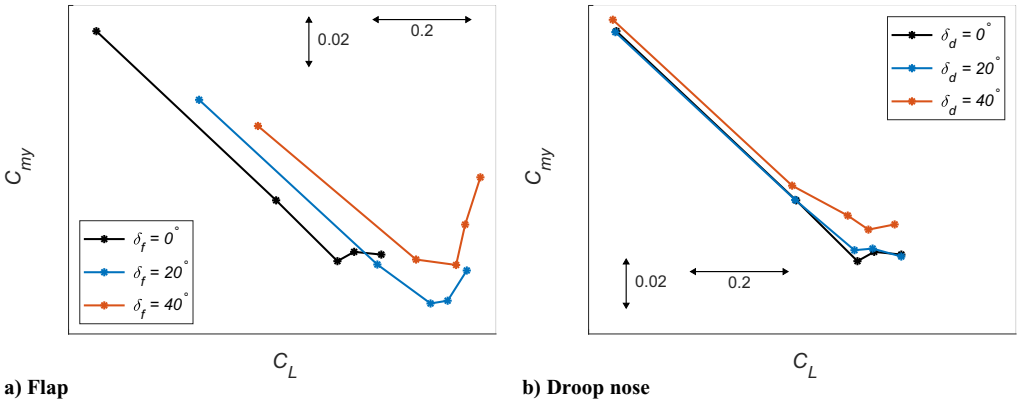
Previous studies [25] have shown that M_∞ should not significantly impact the dynamic coefficients; for this reason, the VLM calibrated with experiments is deemed sufficient here. It is possible to perform unsteady RANS simulations to determine the aerodynamic dynamic coefficients, as in [26,27]; however, these studies show a limited impact of M_∞ in the flight conditions considered in this work.

As seen so far, the control authority of the control surfaces tends to decrease with increasing angle of attack. At low speed, where higher angles of attack may be required, the control authority of the control surfaces could be insufficient to maneuver the aircraft. A possible solution is to include a high-lift flap, which would decrease the required angle of attack while providing the necessary lift, as shown in [21]. The impact of the high-lift flap considered in Fig. 9a is depicted in Fig. 15. The high-lift device is modeled as a plain flap, and, for simplicity reasons, it is supposed to extend along the entire inner wing trailing edge. The setup tested here is not representative of the final design of the aircraft. However, it is used to understand the impact of such a control surface.

Figure 15a shows the impact of two high-lift flap deflections $\delta_f = 20$ and 40 deg on C_{my} as a function of C_L. The simulations are conducted at $M_\infty = 0.2$, and each point corresponds to a fixed angle of attack. As expected, the high-lift flap deflection increases the lift at fixed α, i.e., the curves move to the right. Considering the curves up to the pitch break, the pitching moment always decreases. However, the pitch break occurs at a lower α for $\delta_f = 40$ deg. Similar to the other control surfaces, the effectiveness of the flaps tends to decrease, in an absolute sense, with α. Because of its location close to the CG, the high-lift device has a relatively small impact on the pitching moment coefficient; hence, it does not induce significant additional requirements for the elevator.

Another option to increase the available $C_{L,\max}$ would be to increase the lift produced by the outer wing, e.g., by employing a droop nose. Figure 15b depicts the impact of the leading-edge droop nose at $\delta_d = 20$ and 40 deg. When compared with the high-lift flap, the droop nose has a minor impact on the lift coefficient; however, it leads to a slight increase in the pitching moment. At the higher deflection case $\delta_d = 40$ deg, the increase in pitching moment leads to a slight postponement of the pitch break at higher C_L. The

Downloaded by Technische Universiteit Delft on November 12, 2026 | http://arc.aiaa.org | DOI: 10.2514/1.C038513



a) Flap **b) Droop nose**

Fig. 15 RANS-predicted effect of high-lift devices on lift and pitching moment coefficients at $M_\infty = 0.2$.

induced change leads to a lower impact on the pitching moment and hence to a smaller requirement for the elevator.

The results presented here for the full-scale aircraft show that the effect of α on the control surfaces' control authority is not straightforward. Hence, assuming superposition of the effects of angle of attack, sideslip angle, and deflection angles would significantly impact the prediction of the forces and moments acting on the aircraft at different flight conditions. Furthermore, the evolution of the coefficients and their derivatives with M_∞ is opposite to what the Prandtl–Glauert compressibility correction would predict, i.e., the control authority decreases, in an absolute sense, with M_∞. Also, at higher angles of attack and $M_\infty \geq 0.7$, the presence of shocks modifies the flow evolution on the wing, directly impacting the effectiveness of the control surfaces. Finally, additional control surfaces, such as a high-lift flap and a droop nose, were tested, showing the ability to increase the available $C_{L,\max}$ at low speed.

V. Conclusions

The present work proposes an aerodynamic model for a full-scale flying wing aircraft by deriving the methodology from a comparison of different methods.

Different experimental and numerical methods were initially compared for a subscale version of the Flying V. The experiments comprised wind tunnel and flight data. The comparison between the two experimental methods showed good agreement, particularly for the most relevant coefficients of the three considered control surfaces, i.e., C_{mx,δ_a}, C_{my,δ_e}, and C_{mz,δ_r}. Because the coefficients are angle-of-attack dependent and the angle-of-attack range cannot be varied in the flight experiments, the experimental data set used for comparison with the numerical methods is obtained by combining the static aerodynamic coefficients from the wind tunnel experiments with the dynamic coefficients from the flight tests.

The numerical methods tested were VLM, the panel method, and RANS simulations. The comparison between experimental and numerical data is composed of 23 experimental aerodynamic coefficients. The comparison showed that the RANS simulations best matched the experimental data for the static coefficients. The VLM best matched the dynamic coefficients; however, significant differences were observed for some coefficients.

Further comparisons analyzed the impact of angle of attack. First, it was shown that RANS simulations can adequately predict the occurrence of pitch break in $C_{my,\alpha}$. Additionally, the simulations were able to predict the change in control surface effectiveness as a function of α, with RANS simulations again better approximating the experimental results. The last comparison conducted on the subscale aircraft showed that the effects of different control surfaces were superposable, also at different α.

Based on the comparison for the subscale aircraft, the aerodynamic model for the full-scale aircraft was determined by combining RANS and VLM simulations. RANS simulations were used to determine the impact of static coefficients and the VLM of the dynamic coefficients. However, because of the discrepancies observed for the subscale aircraft, the VLM-calculated dynamic coefficients were calibrated with the flight data.

The full-scale aircraft simulations were conducted at different Mach numbers M_∞ and altitudes. Furthermore, each coefficient was also simulated at different α. The pitch break occurred at lower lift coefficients as M_∞ increased. The aerodynamic coefficients tended to decrease, in absolute value, with increasing angle of attack. However, some discrepancies from this trend were observed at transonic conditions. Overall, the results showed a different trend than that predicted by the Prandtl–Glauert transformation, even at low angles of attack and subsonic cases. Finally, at low speed, a high-lift flap located on the inner wing showed the ability to postpone the pitch break occurrence at higher lift coefficients.

Acknowledgments

This publication is part of the project Flying V Flight Control, project number 19511 of the research program Open Technology Programme, which is partly financed by the Dutch Research Council (Nederlandse Organisatie voor Wetenschappelijk Onderzoek). The authors would like to acknowledge the in-kind contributions of KLM Royal Dutch Airlines and ADSE Consulting & Engineering BV. Furthermore, the authors would like to thank Malcom Brown for his help with the wind tunnel experiment.

References

[1] Miller, J. D., and Façanha, C., "The State of Clean Trnasport Policy—A 2014 Synthesis of Vehicle and Fuel Policy Developments," The International Council on Clean Transportation TR, Washington, D.C., 2014.

[2] European Commission: Directorate-General for Research and Innovation and Directorate-General for Mobility and Transport, "Flightpath 2050—Europe's Vision for Aviation – Maintaining Global Leadership and Serving Society's Needs," Publications Office TR KI-31-11-098-EN-C, Brussels, Belgium, 2011, https://data.europa.eu/doi/10.2777/50266.

[3] Mosca, V., Karpuk, S., Sudhi, A., Badrya, C., and Elham, A., "Multidisciplinary Design Optimisation of a Fully Electric Regional Aircraft Wing with Active Flow Control Technology," *Aeronautical Journal*, Vol. 126, No. 1298, 2022, pp. 730–754. https://doi.org/10.1017/aer.2021.101

[4] Frediani, A., Cipolla, V., and Rizzo, E., "The PrandtlPlane Configuration: Overview on Possible Applications to Civil Aviation," *Variational Analysis and Aerospace Engineering: Mathematical Challenges for Aerospace Design*, Springer, Boston, MA, 2012, pp. 179–210. https://doi.org/10.1007/978-1-4614-2435-2_8

[5] Liebeck, R. H., "Design of the Blended Wing Body Subsonic Transport," *Journal of Aircraft*, Vol. 41, No. 1, 2012, pp. 10–25. https://doi.org/10.2514/1.9084

[6] Martínez-Val, R., Pérez, E., Alfaro, P., and Pérez, J., "Conceptual Design of a Medium Size Flying Wing," *Proceedings of the Institution of Mechanical Engineers, Part G: Journal of Aerospace Engineering*, Vol. 221, No. 1, 2007, pp. 57–66. https://doi.org/10.1243/09544100JAERO90

Downloaded by Technische Universiteit Delft on November 12, 2026 | http://arc.aiaa.org | DOI: 10.2514/1.C038513

[7] Park, J., Choi, J.-Y., Jo, Y., and Choi, S., "Stability and Control of Tailless Aircraft Using Variable-Fidelity Aerodynamic Analysis," *Journal of Aircraft*, Vol. 54, No. 6, Nov.–Dec. 2017, pp. 2148–2164. https://doi.org/10.2514/1.C034052

[8] Paul, M., and Rein, M., "Transonic Numerical and Experimental Evaluation of Unconventional Lambda Wing Control Surfaces," *Journal of Aircraft*, Vol. 54, No. 3, 2017, pp. 1139–1149. https://doi.org/10.2514/1.C034080

[9] Benad, J., *The Flying V—A New Aircraft Configuration for Commercial Passenger Transport*, Deutscher Luft-und Raumfahrtkongress, Rostock, Germany, 2015, pp. 1–8. https://doi.org/10.25967/370094

[10] Laar, Y., Atherstone, D., Benad, J., and Vos, R., "Aerodynamic Design of a Flying V Aircraft in Transonic Conditions," *AIAA SciTech*, AIAA Paper 2024-2669, Jan. 2024. https://doi.org/10.2514/6.2024-2669

[11] Yazdi, R. R., Reist, T. A., and Zingg, D. W., "Aerodynamic Optimization of a Flying V Aircraft Based on the Reynolds-Averaged Navier-Stokes Equations," *AIAA SCITECH 2024 Forum*, AIAA Paper 2024-1909, 2024. https://doi.org/10.2514/6.2024-1909

[12] Oosterom, W., and Vos, R., "Conceptual Design of a Flying-V Aircraft Family," *AIAA SciTech*, AIAA Paper 2022-3200, Jan. 2021. https://doi.org/10.2514/6.2022-3200

[13] van der Toorn, M., "Flying-V Family—Design for Stability and Control," Master Thesis, Technische Universiteit Delft, Delft, The Netherlands, 2022.

[14] Palermo, M., and Vos, R., "Experimental Aerodynamic Analysis of a 4.6%-Scale Flying-V Subsonic Transport," *AIAA SciTech*, AIAA Paper 2022-0713, 2020. https://doi.org/10.2514/6.2022-0713

[15] García, A. R., Brown, M., Atherstone, D., van Arnhem, N., and Vos, R., "Aerodynamic Model Identification of the Flying V from Sub-Scale Flight Test Data," *AIAA SciTech*, AIAA Paper 2022-0713, 2022. https://doi.org/10.2514/6.2022-0713

[16] Plaetschke, E., and Schulz, G., "Practical Input Signal Design," Lecture Series No. 104—Parameter Identification—Paper 3, AGARD TR, Neuilly-sur-Seine, France, 1979.

[17] Simmons, B. M., Geuther, S., and Ahuja, V., "Validation of a Mid-Fidelity Approach for Aircraft Stability and Control Characterization," *AIAA AVIATION 2023 Forum*, AIAA Paper 2023-4076, 2023.

[18] Asaro, S., and Vos, R., "Synthesis of the Aerodynamic Model of a Flying Wing Aircraft," *AIAA SciTech*, AIAA Paper 2025-0852, Jan. 2025. https://doi.org/10.2514/6.2025-0852

[19] Huber, K. C., Schütte, A., Rein, M., and Löser, T., "Experimental Aerodynamic Assessment and Evaluation of an Agile Highly Swept Aircraft Configuration," *CEAS Aeronautical Journal*, Vol. 8, No. 1, 2017, pp. 17–29. https://doi.org/10.1007/s13272-016-0219-y

[20] Cui, Z., Lai, G., Wang, Q., Liang, Y., and Cao, Y., "Wind Tunnel Investigation of Different Engine Layouts of a Blended-Wing-Body Transport," *Chinese Journal of Aeronautics*, Vol. 36, No. 9, 2023, pp. 123–132. https://doi.org/10.1016/j.cja.2023.04.027

[21] Asaro, S., Atmaca, D., van Kampen, E.-J., and Vos, R., "Control Surface Allocation Based on Offline Handling Quality Simulations for a Flying Wing Aircraft," *CEAS Aeronautical Journal*, Oct. 2025. https://doi.org/10.1007/s13272-025-00906-2

[22] Nangia, R., Ghoreyshi, M., van Rooij, M. P., and Cummings, R. M., "Aerodynamic Design Assessment and Comparisons of the MULDICON UCAV Concept," *Aerospace Science and Technology*, Vol. 93, Oct. 2019, Paper 105321. https://doi.org/10.1016/j.ast.2019.105321

[23] Shim, H., and Park, S.-O., "Passive Control of Pitch-Break of a BWB UCAV Model Using Vortex Generator," *Journal of Mechanical Science and Technology*, Vol. 29, No. 3, 2015, pp. 1103–1109. https://doi.org/10.1007/s12206-015-0222-y

[24] Asaro, S., Khalil, K., and Bauknecht, A., "Unsteady Characterization of Fluidic Flow Control Devices for Gust Load Alleviation," *New Results in Numerical and Experimental Fluid Mechanics XIII*, Springer, Cham, Switzerland, 2021, pp. 153–163. https://doi.org/10.1007/978-3-030-79561-0_15

[25] Winchenbach, G. L., Uselton, B. L., Vathaway, W. H., and Chelekis, L. R., "Comparison of Free-Flight and Wind Tunnel Data for a Generic Fighter Configuration," *AlAA 9th Atmospheric Flight Mechanics Conference*, AIAA Paper 1982-1365, 1982.

[26] Ghoreyshi, M., and Cummings, R. M., "Unsteady Aerodynamics Modeling for Aircraft Maneuvers: A New Approach Using Time-Dependent Surrogate Modeling," *Aerospace Science and Technology*, Vol. 39, Dec. 2014, pp. 222–242. https://doi.org/10.1016/j.ast.2014.09.009

[27] Da Ronch, A., Ghoreyshi, M., Badcock, K., and Vallespin, D., "Computation of Dynamic Derivatives Using CFD," *28th AIAA Applied Aerodynamics Conference*, AIAA Paper 2010-4817, 2010. https://doi.org/10.2514/6.2010-4817

A. Broeren
Associate Editor

Downloaded by Technische Universiteit Delft on November 12, 2026 | http://arc.aiaa.org | DOI: 10.2514/1.C038513